Accepted Manuscript

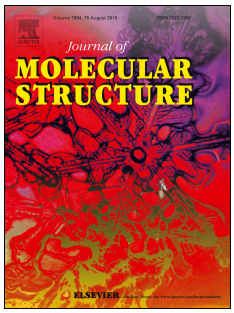

Monoalkylated barbiturate derivatives: X-ray crystal structure, theoretical studies, and biological activities

Assem Barakat, Abdullah Mohammed Al-Majid, Saied M. Soliman, Mohammad Shahidul Islam, Hussain Mansur Ghawas, Sammer Yousuf, M. Iqbal Choudhary, Abdul Wadood

PII: S0022-2860(17)30448-9

DOI: 10.1016/j.molstruc.2017.04.017

Reference: MOLSTR 23639

To appear in: *Journal of Molecular Structure*

Received Date: 14 March 2017

Revised Date: 4 April 2017

Accepted Date: 6 April 2017

Please cite this article as: A. Barakat, A.M. Al-Majid, S.M. Soliman, M.S. Islam, H.M. Ghawas, S. Yousuf, M.I. Choudhary, A. Wadood, Monoalkylated barbiturate derivatives: X-ray crystal structure, theoretical studies, and biological activities, *Journal of Molecular Structure* (2017), doi: 10.1016/j.molstruc.2017.04.017.

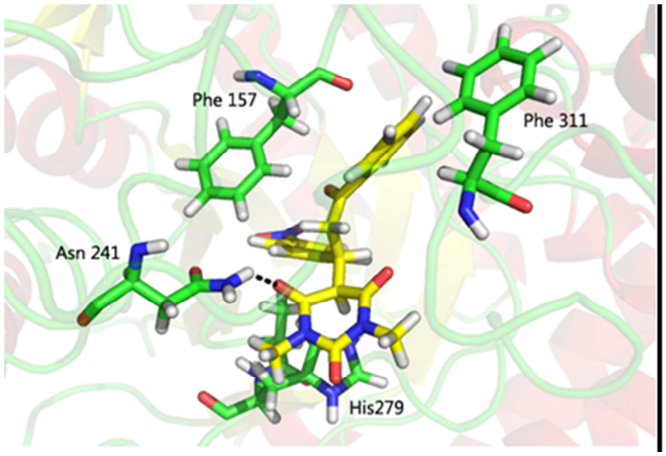

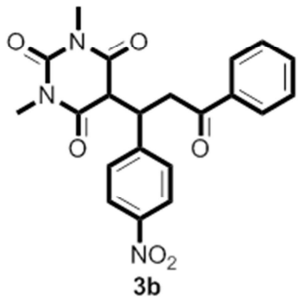

3b

DPPH: (IC_{50} = 91.223±0.75 µM)

α-Glucosidase Inhibition: (IC_{50} = 133.1±3.2 µM)

Monoalkylated barbiturate derivatives: X-Ray crystal structure, theoretical studies, and biological activities

Assem Barakat[1,3,*], Abdullah Mohammed Al-Majid[1], Saied M. Soliman[2,3], Mohammad Shahidul Islam[1], Hussain Mansur Ghawas[1], Sammer Yousuf[3], M. Iqbal Choudhary[1,4], and Abdul Wadood[5]

[1] Department of Chemistry, College of Science, King Saud University, P. O. Box 2455, Riyadh 11451, Saudi Arabia.

[2] Department of Chemistry, College of Science & Arts, King Abdulaziz University, P.O. Box 344 Rabigh 21911, Saudi Arabia.

[3] Department of Chemistry, Faculty of Science, Alexandria University, P.O. Box 426, Ibrahimia, Alexandria 21321, Egypt.

[4] H.E.J. Research Institute of Chemistry, International Center for Chemical Sciences, University of Karachi, Karachi 75270, Pakistan.

[5]Department of Biochemistry, Abdul Wali Khan University, Mardan-23200, Pakistan. (A.W)

***** Correspondence: ambarakat@ksu.edu.sa; Tel.: +966-114-675-901; Fax: +966-114-675-992.

Abstract: Barbiturate derivatives are privileged structures with a broad range of pharmaceutical applications. We prepared a series of 5-monoalkylated barbiturate derivatives (**3a–l**) and evaluated, *in vitro*, their antioxidant (DPPH assay), and α-glucosidase inhibitory activities. Compounds **3a–l** were synthesized *via* Michael addition. The structure of compound **3k** was determined using X-ray single-crystal diffraction, and geometric parameters were calculated using density functional theory at the B3LYP/6-311G(d,p) level of theory. Further, the structural analysis of **3k** were also investigated. Biological studies revealed that compounds **3b** (IC_{50} = 133.1 ± 3.2 µM), **3d (**IC_{50} = 305 ± 7.7 µM), and **3e** (IC_{50} = 184 ± 2.3 µM) have potent α-glucosidase enzyme inhibitors and showed greater activity than the standard drug acarbose (IC_{50} = 841 ± 1.73 µM). Compounds **3a**–**3i** were found to show weak antioxidant activity against

1,1-diphenyl-2-picryl-hydrazyl (DPPH) radicals (IC_{50} = 91 ± 0.75 to 122 ± 1.0 µM) when tested against a standard antioxidant, gallic acid (IC_{50} = 23 ± 0.43 µM).

Keywords: Barbituric acid; DFT; antioxidant (DPPH); *α*-Glucosidase Inhibitors.

1. Introduction

The 5-alkylbarbiturate structural motif has been found in several synthetic and natural products with pharmaceutical activity such as antitumor, immunomodulating [1], sedative [2], and anticonvulsant properties [3]. Additionally, several monoalkyl barbiturates have been used in supramolecular chemistry [4], nonlinear optical studies [5], and manufacture of dyes [6]. For example, 5-alkylbarbiturates inhibit matrix metalloproteinase (MMP) completely [7], while the compound PNU-286607(-)-1 is an antibacterial agent [8] and prevents mutant SOD1-dependent protein aggregation [9]. Thus, taking into consideration the potential pharmaceutical activity of the 5-alkylbarbiturate structural system, the construction of complex molecular frameworks incorporating this privileged structure is an interesting goal. Toward this, different approaches have recently been disclosed, enabling the construction of 5-monoalkylbarbiturates [10–17]. For example; 5-monoalkylated barbituric acid derivative were identified as α-glucosidase inhibitors [18-21].

As part of our continuing research program, we report the synthesis of a series of 5-monoalkylbarbiturate derivatives and evaluate these *in vitro* with a DPPH radical scavenging assay and for their*α*-glucosidase inhibition. Quantum chemical calculations were performed to analyze the structure and electronic and spectroscopic aspects of the studied compounds in the framework of density functional theory (DFT) at the B3LYP/6-311G(d,p) level of theory.

2. Results and discussion

2.1. Synthesis

The synthesis of the 5-monoalkylbarbiturate derivatives is depicted in Scheme 1. Equimolar *N*,*N*-dimethyl barbituric acid (**1**) and chalcone derivatives (**2a–l**) in dichloromethane (DCM) in the presence of diethylamine ($NHEt_2$) base gave the desired 5-monoalkylbarbiturate derivatives (**3a–l)** in good yields. The yields of the 5-monoalkylbarbiturate derivatives were consistent with reported data [17]. Furthermore, the molecular structure of **3k** was confirmed by single crystal X-ray diffraction.

Scheme 1. Preparation of 5-mono alkyl barbiturate derivatives **3a–l**

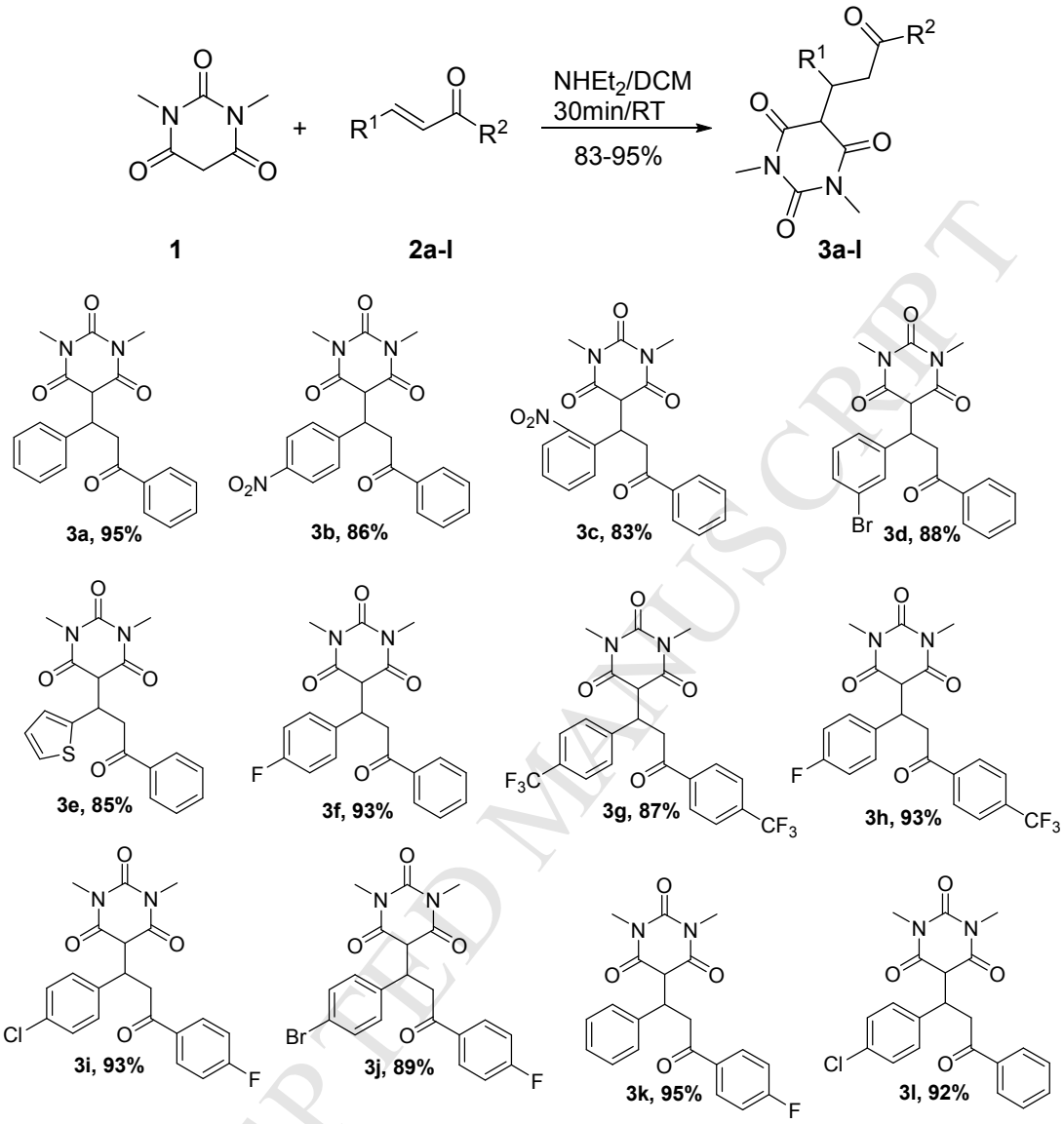

2.2. X-ray crystal structure of compound 3k

The solid-state structure of compound **3k** was determined by single-crystal X-ray diffraction. The crystal and structure refinement data, as well as selected geometric parameters for compound **3k**, are given in Tables 1 and 2. The asymmetric unit comprises two independent molecules of **3k**. The pyrimidine (N1/N3/C2/C4-C6), fluorophenyl (C12-C17), and phenyl (C18-C23) rings are planar with a maximum root mean squared deviation (RMSD) from the mean plane of 0.145(3) Å for C5 (Fig. 1). The two phenyl rings (C12-C17 and C18-C23) were found to be twisted by 12.8(2)° and 37.7(2)°, respectively, with respect to the plane of the pyrimidine ring. In the crystal, molecules are linked by C7–H7B···O6, C7–H7C···O4, C8–H8B···F1, C13–H13A···O4, C37–H37A···F2,

C39–H39A···O8, and C40–H40A···O7 intermolecular interactions, resulting in a three-dimensional network structure (Fig. 2 and Table 3) [22–24].

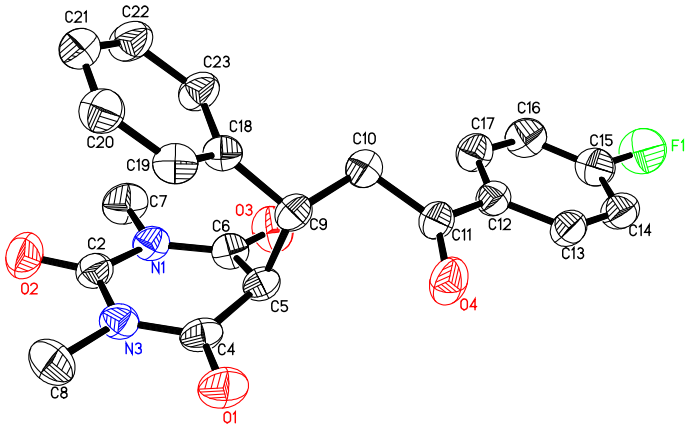

Fig. 1 ORTEP diagram of the compound **3k**. Displacement ellipsoids are plotted at the 30% probability level.

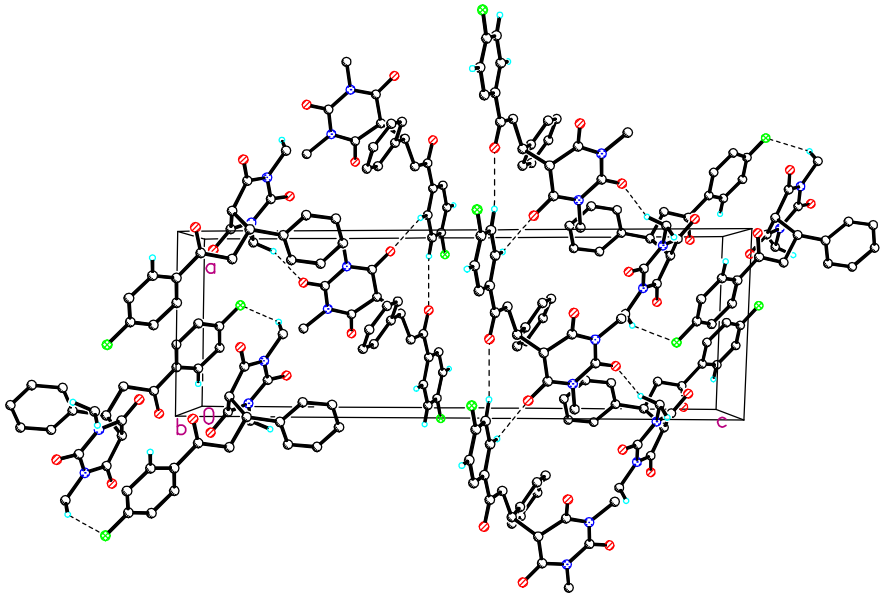

Fig. 2 Crystal packing showing intermolecular C---H….O hydrogen bonds as dashed lines.

Table 1. Crystal data and structure refinement for compound **3k**

Crystal data	**3K**
Empirical Formula	$C_{42}H_{38}F_2N_4O_8$
Formula Weight	764.76

Temperature (K)	293(2)
Wavelength (Å)	0.71073
Crystal system	Triclinic
Space group	P1
Unit cell dimensions	*a* = 7.9163(9) Å, α = 283.111(2)°
	b = 8.9021(10)Å, β = 287.831(2)°
	c =24.079(3)Å, γ = 72.8270 (10)°
Volume ($Å^3$)	1676.0(3)
Z, catculated density ($Mg.m^{-3}$)	2, 1.515
Absorption coefficient (mm^{-1})	0.113
F(000)	800
Crystal size (mm)	0.59 x 0.52 x 0.22
Theta range for data collection (°)	0.85° to 25.50 °
Limiting indices	-9≤h≤9, -10≤k≤10, -29≤l≤29
Reflections collected /unique	18870 / 6247 [R(int) = 0.0609]
Completeness to theta	25.50 (100 %)
Refinement method	Full-matrix least-squares on F^2
Data/ restraints/ parameters	6247 / 0 / 506
Goodness of- fit on F^2	0.981
Final R indices [I>2σ(I)]	R1 = 0.0625, wR2 = 0.1540
R indices (all data)	R1 = 0.1463, wR2 = 0.2077
Largest diff. peak and hole (e A^{-3})	0.239 and -0.249
CCDC reference	1024287

Table 2 Selected geometric parameters (Å, °) of **3k**

O1—C4	1.177(4)	O3—C6	1.169(4)

O2—C2	1.163(4)	O4—C11	1.181(4)
O5 —C24	1.174(4)	O6 —C26	1.154(4)
O7— C28	1.175(4)	O8 —C34	1.172(4)
F1 —C15	1.317(5)	F2— C38	1.313(4)
N1 —C6	1.327(5)	N1 —C2	1.329(5)
N1 —C7	1.408(4)	N3 —C4	1.318(5)
N3 —C2	1.337(5)	N3 —C8	1.414(5)
N25— C24	1.317(4)	N25 —C26	1.328(4)
N25— C30	1.423(4)	N27 —C28	1.311(4)
N27— C26	1.329(5)	N27 —C31	1.418(4)
C6 —N1— C2	124.1(3)	C6 —N1— C7	118.0(4)
C2 —N1— C7	117.9(4)	C4— N3 —C2	123.2(4)
C4— N3— C8	119.2(3)	C2 —N3— C8	117.5(4)
C24— N25 —C26	123.8(3)	C24 —N25— C30	118.8(3)
C26 —N25 —C30	117.4(3)	C28— N27 —C26	123.9(3)
C28— N27— C31	118.5(4)	C26— N27— C31	117.5(3)
O2— C2— N1	121.0(4)	O2— C2— N3	121.0(4)
N1 —C2 —N3	118.0(4)	O1 —C4— N3	120.2(4)
O1— C4 —C5	121.9(4)	N3— C4— C5	117.9(3)
O4 —C11— C12	120.2(4)	O4 —C11— C10	119.1(4)

Table 3. Hydrogen-bond geometry (Å, °) of **3k**

D—H···A	D—H	H···A	D···A	D—H···A
C7—H7B···O6i	0.96	2.31	3.136(6)	143
C7—H7C···O4 ii	0.96	2.57	3.360(5)	140
C8—H8B···F1 iii	0.96	2.39	3.219(5)	145
C13—H13A···O4iv	0.93	2.25	3.096(5)	152
C37—H37A···F2v	0.93	2.39	3.196(5)	144
C39—H39A···O8i	0.93	2.52	3.406(5)	159
C40—H40A···O7i	0.93	2.29	3.022(5)	136

Symmetry code: (i) -1+x,y,z, (ii) x,-1+y,z (iii) -x,2-y,-z, (iv) -x,3-y,-z, (v) -x,-1-y,1-z,

2.3. Computational details

Geometry optimization of **3k** followed by frequency analysis was performed at the B3LYP/6-311G(d,p) level of theory using Gaussian 03, revision C.01 [25]. The X-ray structure coordinated taken from the crystallographic information file is used as starting input for our calculations. All vibrational modes were positive, and no imaginary frequency modes were detected. Time-dependent (TD)-DFT and gauge-including atomic orbital (GIAO) NMR chemical shifts calculations at the optimized geometry were performed to predict the electronic and NMR spectra of the studied compound. The ^{13}C and ^{1}H chemical shifts (δ) were calculated using the GIAO isotropic magnetic shielding (IMS) values based on the equation: $CS_x = IMS_{TMS} - IMS_x$.

All calculations were made without symmetry restrictions. The optimized structure was drawn with the aid of Chemcraft [26]. The frontier molecular orbital (FMO) pictures as well as the molecular electrostatic potential (MEP) map were drawn using Gaussview 4.1 [27]. GaussSum 2.2 [28] was used to obtain the molecular orbital contributions of the studied electronic transitions. The natural charges and the intramolecular charge transfer interaction energies were deduced from natural bond orbital (NBO) analysis using NBO 3.1 [29]. The

global chemical reactivity descriptors such as electronegativity (χ), chemical potential (μ), chemical hardness (η), global softness (S) and global electrophilicity index (ω) were calculated using Eqs. (1)–(5) [30-34].

$$\chi = \frac{(I + A)}{2}, \quad (1)$$

$$\mu = -\chi = -\frac{(I + A)}{2}, \quad (2)$$

$$\eta = \frac{(I - A)}{2}, \quad (3)$$

$$S = \frac{1}{2\eta}, \quad (4)$$

$$\omega = \frac{\mu^2}{2\eta}, \quad (5)$$

where*I* and *A* are the ionization potential and electron affinity, respectively, which are defined as the negative values of the E_{HOMO} and E_{LUMO}, respectively.

2.4. Structure

The minimum energy structure obtained from the geometry optimization of the X-ray structure of **3k** at the B3LYP/6-311G(d,p) level of theory is shown in Fig. 3. The molecular point group is C1. The calculated and experimental bond distances and bond angles are presented in Figs. S1–S2 and Table S1 (Supplementary Data). In this table, the statistical parameters such as RMSD and correlation coefficients indicate a good agreement between the calculated and experimental geometrical parameters. The maximum bond distance and bond angle deviations from the experimental values are 0.087 Å and 3.4° for C30-C32 and C12-C10-C21, respectively. The deviations of the calculated geometric parameters are mainly due to phase differences between calculation and experiment. That is, the calculations were performed on a single molecule in the gas phase, whereas, in a single crystal (as used for the X-ray experiments) molecular packing effects are present. In the crystal, there are many intermolecular interactions that affect the geometric parameters, resulting in deviations from the gas-phase structure. Despite these differences, the geometric parameters correlate well with the experimental data, and the bond distances offer a better agreement with the experimental data than the bond angle values.

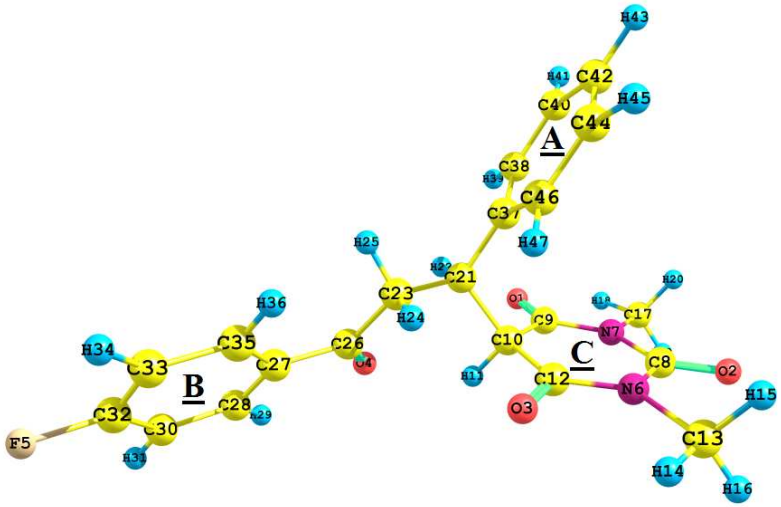

Fig. 3 The calculated molecular structure of **3k** using B3LYP/6-311G(d,p) method.

2.5. Natural atomic charges

Most of the electronic properties of a molecule, such as the dipole moment, molecular polarizability, electronic structure, and molecular reactivity, are related to the charge distribution at the different atomic sites. The charges on the atoms of the compound were calculated using the NBO method at the B3LYP/6-311G(d,p) level of theory. The results are presented graphically in Fig. 4. Almost all the C-atoms of the phenyl rings have negative natural charges. However, C32 has high positive charge, which is attributed to its attachment to a highly electronegative F-atom. For the pyrimidinetrione ring, all C-atoms (except C10) are electropositive because they are attached to either O and N-atoms or both. The most electropositive C-atom is C8 (0.8500), and this is because C8 is bonded to three highly electronegative atoms. Moreover, all H-atoms have positive charge densities, where the most electropositive H-site is H11 (0.2915). The high positive charge density at H11 and the high negative charge density at C10 (-0.3900) are strong indications on the acidic character of the C10-H11 bond.

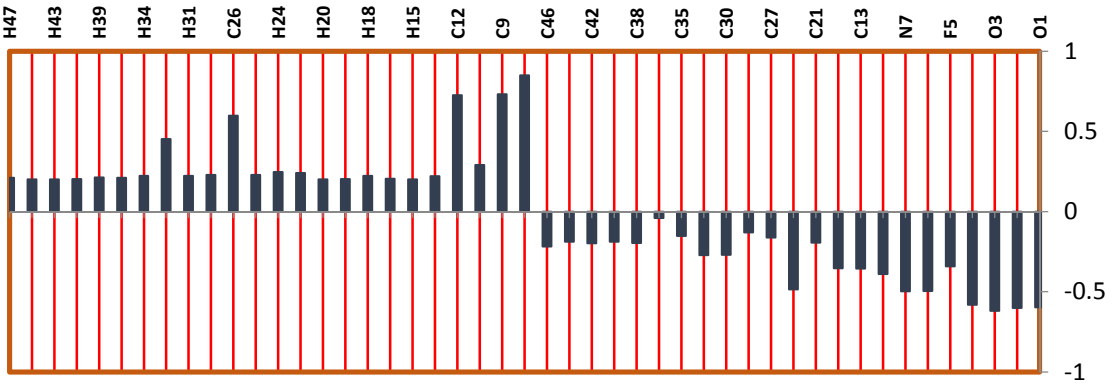

Fig. 4 The natural charge distribution at the different atomic sites of the studied molecule.

2.6. Molecular electrostatic potential

An MEP map was calculated for the B3LYP/6-311G(d,p) optimized geometry (Fig. S3; Supplementary Data). This three-dimensional map is colored according to the electrostatic potential: deep red for electron rich regions and deep blue for electron poor regions. The reddest regions are those most reactive to attack by an electrophile, while the bluest regions are electrophilic sites. MEP maps can be used to determine how molecules interact with one another [35, 36]. The MEP map shows that negative charge is concentrated at the top of the carbonyl O-atoms as well as the F-atom. The positive regions spread over the surface of the hydrogen atoms. It is clear also from this map that the phenyl ring C-skeleton (yellow) is more electron rich than the pyrimidine trione core (blue). Hence, the former favors electrophile attack, while the latter favors nucleophilic attack [37].

2.7. HOMO–LUMO analysis

The highest occupied molecular orbital (HOMO) and lowest occupied molecular orbital (LUMO) are the FMOs. The HOMO energy is indicative of the ability of a molecule to donate electrons. On the other hand, the LUMO energy gives an indication of the ability of a molecule to accept electrons. Moreover, the HOMO-LUMO energy difference is defined as the transition energy. This energy gap yields information on the ease of electronic transitions. A large energy gap (ΔE) indicates high stability with respect to electron transfer. In addition, these FMOs are related to the electric and optical properties,

as well as the chemical reactivity [38].For **3k**, E_{HOMO} = -7.0271 eV, E_{LUMO} = -1.8806 eV, and ΔE = 5.1465 eV.

The FMOs are shown in Fig. S4 (Supplementary data). Both HOMO and LUMO are mainly distributed over the π-system of the molecule. The HOMO level is mainly localized over the phenyl ring A and C26=O4 π-systems, while the LUMO is localized over ring B. From this point of view, ring A acts as the electron rich fragment and acts as an electron donor while ring B, which carries the very electronegative F-atom, is an electron acceptor. Hence, the electronic transition could be described as a π-π* transition from ring A to B. The energy of this electronic transition (5.1465 eV) is relatively high, indicating that the studied compound is highly stable.

2.8. Chemical properties

Based on the HOMO and LUMO energies, the chemical reactivity descriptors such as chemical potential (μ), electronegativity (χ), chemical hardness (η), global softness (S), and global electrophilicity index (ω) were calculated, and the results are presented in Table 4. The chemical potential can be used to describe many electrical and nuclear properties [39], and it reflects a molecule's propensity for spontaneous chemical decomposition. Hence, if the chemical potential is negative, a compound is stable and does not decompose spontaneously [40]. The chemical hardness (μ) indicates the ability of a molecular system to resist polarization. High values of μ indicate a less polarized system and, hence, greater stability against electronic deformation under small perturbations during a chemical reaction, and softness is the reverse of hardness. The electrophilicity index (ω) indicates the ability of a molecule to gain electrons from the environment, that is, its ability to act as an electrophile [41]. The high electrophilicity index indicates the high electrophilic character of the studied compound, which is probably due to the presence of a large number of highly electronegative atoms.

Table 4 The E_{HOMO}, E_{LUMO} and the derived chemical reactivity descriptors of **3k** calculated by B3LYP/6-31G(d,P) method.

Parameter	Energy (eV)
E_{HOMO}	-7.0271

E_{LUMO}	-1.8806
chemical potential (μ)	- 4.4539
electronegativity (χ)	4.4539
chemical hardness (η)	2.5733
global softness (S)	0.1943
global electrophilicity index (ω)	3.8544

2.9. Electronic spectra of the studied compound

The electronic spectrum of **3k** was calculated using TD-DFT, and the results of the forty singlet-singlet electronic transitions are given in Table S2 (Supplementary Data). Theoretical and experimental ultraviolet-visible (UV-Vis) spectra are shown in Fig. S5 (Supplementary Data). Experimentally, the spectrum of **3k** in acetonitrile contains three electronic transition bands at 203, 237, and 303 nm, as well as a shoulder at 265 nm. Theoretically, the two intense electronic transitions were predicted at 203.9 nm (*f* = 0.1185) and 244.0 nm (*f* = 0.3377), which agree with the experimental data. The most intense and longest wavelength band was assigned to the H-2→L (80%) transition, while the shorter wavelength band arises from the H-5→L (22%), H-2→L+2 (56%) excitations. The molecular orbitals involved in these electronic transitions are shown in Fig. 5. Both electronic transitions are π→π* excitations.

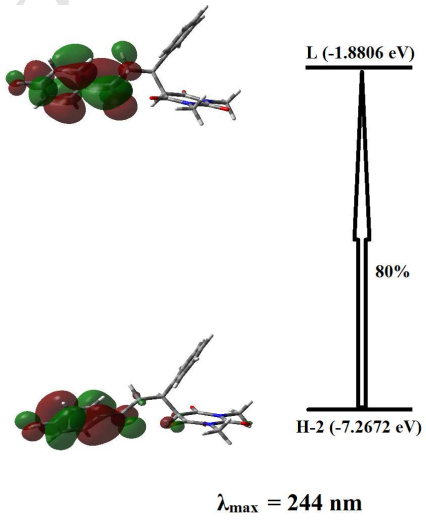

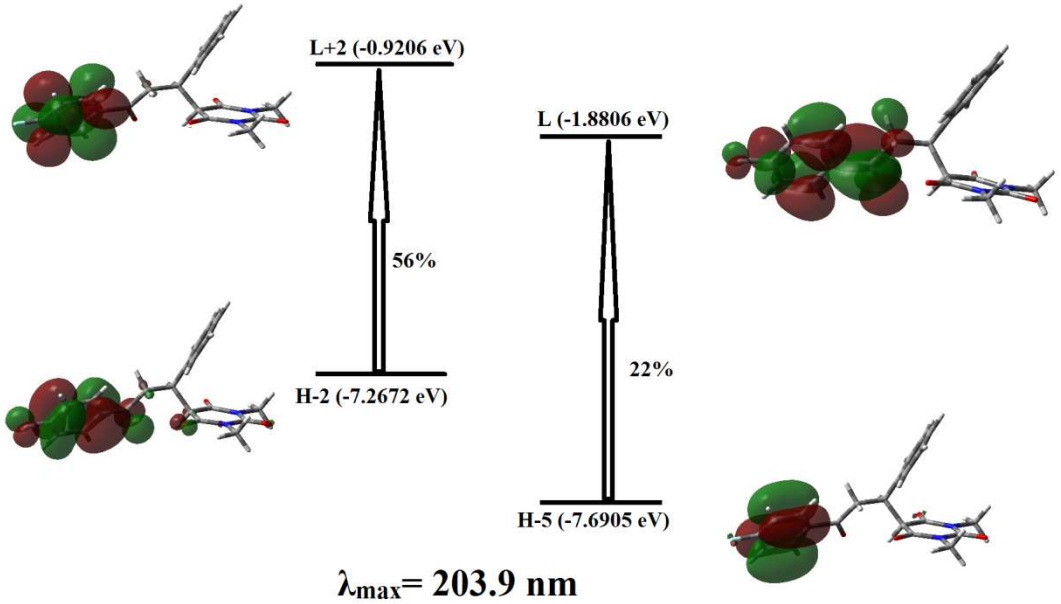

Fig. 5 The molecular orbitals involved in the most important electronic transition bands calculated using TD-DFT method at B3LYP/6-311G(d,p).

2.10. Natural bond orbital (NBO) analyses

The NBO analyses presented in this section show the most accurate Lewis structural description of **3k**. For each A-B bond, the electron occupancy (ED), the percentage electron density at each atom (ED%), and the polarization coefficients of each atom forming the bond, as well as the composition of the atomic orbitals in the bond hybrids, are presented in Table S3 (Supplementary Data). For all C-H bonds, all H-atoms have 0% p-character. In contrast, BD(2)C=C and BD(2)C=O π-NBOs have almost 100% p-character. Similarly, LP(1)N, LP(2)F, LP(3)F, and LP(2)O NBOs have 100% p-character.

For **3k**, the BD(1)C10-C21 with 1.9391 electrons has a 52.17% electron density at C10 (27.18% s) and 47.83% electron density at C21 (24.40% s). The high s-character at C10 indicates the high acidity of the C10-H11 bond. Moreover, the BD(1)C21-C23 NBO with 1.9710 electrons has 50.12% ED at C21 (27.01% s) and 49.88% ED at C23(29.50% s). The BD(1)C21-C23 has almost two C-atoms of equal electron density and hence almost equal polarization coefficients (0.7080 and 0.7063), while C10 of the BD(1)C10-C21 NBO has a higher electron density than that of C21. As a result, C10 (0.7223) has a higher polarization coefficient than that of C21 (0.6916). In addition, all C-O, C-N, and C-F bonds have higher

polarization coefficients at the O, N, and F-atoms, respectively, compared to carbon. The polarization coefficients at the O, N, and F atoms are 0.8091–0.8139, 0.7924–0.8025, and 0.8540, respectively. Fluorine has the highest electronegativity.

The stabilization energy ($E^{(2)}$), which results from the delocalization of electrons among bonds, is an important quantitative measure of the stability of a molecular system. Using second-order perturbation theory and NBO analysis, the stabilization energies ($E^{(2)}$) due to the most important intramolecular charge transfer (ICT) interactions from the donor NBO to the acceptor were determined, and these are given in Table 5. The stabilization energies ($E^{(2)}$) arising from the π→π* ICT interactions range from 16.36 to 25.21 kcal/mol. Of these π→π* ICT interactions, the strongest interaction is π(C28-C30)→ π*(C32-C33) in ring B, which has an F-substituent. The presence of such a strongly electronegative atom at C32 increases the ICT to the sπ*(C32-C33) antibonding NBO to a greater degree than the other ICTs Moreover, the π(C27-C35)→π*(O4-C26) ICT has an $E^{(2)}$ value of 18.91 kcal/mol, indicating strong electron delocalization from the π(C27-C35) NBO of ring A, which acts as a donor to the π*-antibonding NBO of the carbonyl group (O4=C26).

The ICTs from the filled lone pair NBO to the adjacent σ*- or π*-NBOs have maximum stabilization energies of 26.66 and 54.23 kcal/mol, respectively. The $n \rightarrow \pi^*$ ICT interactions stabilize the system more than the $n \rightarrow \sigma^*$ ICT interactions, and the $n \rightarrow \sigma^*$(C-N) ICT interactions are stronger than those of the $n \rightarrow \sigma^*$(C-C) ICTs.

Table 5. The most important intramolecular charge transfer interactions and their stabilization energies deduced from the second order perturbation theory.

Donor NBO	Acceptor NBO	$E^{(2)}$ (kcal/mol)	Donor NBO	Acceptor NBO	$E^{(2)}$ (kcal/mol)
BD(2)C27-C35	BD*(2)O4-C26	18.91	LP(2) O1	BD*(1)N7-C9	26.66
BD(2)C27-C35	BD*(2)C28-C30	21.69	LP(2) O1	BD*(1)C9-C10	19.27
BD(2)C27-C35	BD*(2)C32-C33	18.42	LP(2) O2	BD*(1)N6-C8	25.86

			LP(2)		
BD(2)C28-C30	BD*(2)C32-C33	25.21	O2	BD*(1)N7-C8	25.49
			LP(2)		
BD(2)C28-C30	BD*(2)C27-C35	17.48	O3	BD*(1)N6-C12	25.85
			LP(2)		
BD(2)C32-C33	BD*(2)C27-C35	22.78	O3	BD*(1)C10-C12	18.10
			LP(2)		
BD(2)C32-C33	BD*(2)C28-C30	16.36	O4	BD*(1)C23-C26	19.36
BD(2)C37-C38	BD*(2)C40-C42	20.67	LP(2)O4	BD*(1)C26-C27	18.88
BD(2)C37-C38	BD*(2)C44-C46	20.23	LP(3)F5	BD*(2)C32-C33	19.75
BD(2)C40-C42	BD*(2)C37-C38	20.54	LP(1)N6	BD*(2)O2-C8	52.59
BD(2)C40-C42	BD*(2)C44-C46	21.04	LP(1)N6	BD*(2)O3-C12	51.96
BD(2)C44-C46	BD*(2)C37-C38	20.84	LP(1)N7	BD*(2)O1-C9	51.26
	BD*(2)C40-				
BD(2)C44-C46	C42	20.00	LP(1)N7	BD*(2)O2-C8	54.23

2.11. NMR spectral analysis

Isotropic chemical shifts are used for the identification of organic compounds. GIAO calculations were used for the accurate prediction of the ^{1}H and ^{13}C isotropic chemical shifts, and these are presented in Table 6. The chemical shifts of the aromatic carbons overlap between 100 and 200 ppm [42]. Atom C32 has a higher chemical shift (calc. 176.01 pm and exp. 167.75 ppm) than the other aromatic carbons (calc. 119.80–149.12 ppm and exp. 130.65–150.87 ppm). The high chemical shift of C32 is due to the deshielding effect of the electronegative F-atom. The oxygen and nitrogen atoms are more electronegative than the carbon atoms, so the carbonyl C-atoms were detected at higher chemical shifts (150.87–196.03 ppm), which is consistent with the calculated values (calc. 156.59–202.30 ppm).

The ^{1}H-chemical shifts of the aromatic ring usually appear in the region of 7 to 8 ppm. In the present study, the aromatic protons were detected at 7.12–8.02 ppm, which is in good

agreement with B3LYP theoretical values (7.15–8.62 ppm). The aliphatic protons have lower chemical shifts than the aromatic ones. The experimentally measured aliphatic ^{1}H-signals are in the range 3.02–4.36 ppm (calc. 2.29–4.83) ppm. Correlation graphs between the experimental and theoretical NMR chemical shifts are shown in Figs. S6 and S7 (Supplementary Data). The correlation equations shown below have high R^2 values (0.932–0.962, indicating a good agreement between the theoretical and experimental data.

$\delta calc = 0.996\ \delta exp - 2.653 \quad R^2 = 0.962 \quad {}^{13}$C-NMR (6)

$\delta calc = 0.899\ \delta exp + 0.387 \quad R^2 = 0.932 \quad {}^{1}$H-NMR (7)

Table 6 The calculated and experimental chemical shifts (^{1}H and ^{13}C) for **3k** using GIAO method at 6-311G(d,p) method.

Atom		δcalc	δexp	Atom		δcalc	δexp
C	8	156.59	150.87	H	11	4.70	3.96
C	9	172.97	197.11	H	14	4.28	3.09
C	10	54.39	52.86	H	15	2.41	3.09
C	12	174.60	167.75	H	16	2.65	3.09
C	13	28.73	28.07	H	18	4.27	3.02
C	17	29.22	27.95	H	19	2.59	3.02
C	21	50.79	40.18	H	20	2.29	3.02
C	23	44.58	44.33	H	22	4.38	4.36
C	26	202.30	196.03	H	24	4.83	4.03
C	27	138.59	137.97	H	25	2.89	3.48
C	28	137.58	115.83	H	29	8.62	8.02
C	30	120.95	130.74	H	31	7.25	7.24
C	32	176.01	167.75	H	34	7.15	7.24
C	33	119.80	130.65	H	36	8.08	8.02
C	35	136.28	115.61	H	39	7.39	7.12
C	37	149.12	150.87	H	41	7.38	7.12
C	38	136.46	128.68	H	43	7.39	7.24
C	40	134.20	128.35	H	45	7.44	7.12

C	42	133.36	127.24	H	47	7.43	7.12
C	44	134.07	130.65				
C	46	132.34	128.68				

2.12. Infrared vibrational spectra

The studied molecule contains 47 atoms with a total of 135 vibrational modes. A complete assignment of these modes is presented based on the total energy distribution (TED) obtained from Veda 4 [43]. The results and their comparison with the experimental values are listed in Table S4 (Supplementary Data). The theoretical and experimental IR spectra of the studied molecule are shown in Figs. S8 and S9 (Supplementary data). The calculated vibrational frequencies were scaled by 0.9670 to correct the calculated harmonic frequencies [44]. Generally, the scaled infrared vibrational frequencies agreed well with the experimental data. The most important modes are now presented based on the TED analysis.

2.12.1. C–H vibrations

The studied molecule has both aromatic and aliphatic C-H bonds. The aromatic C-H stretching modes have higher wavenumbers than the aliphatic C–H stretching vibrations. In the present case, the four C-H stretching modes of the phenyl ring B were predicted to have the highest wavenumbers (3102–3087 cm^{-1}), while, in the experimental spectrum, these stretching modes were observed in the range of 3093–3072 cm^{-1}. In contrast, the C-H stretching modes of ring A were predicted by the TED analysis to occur at lower vibrational wavenumbers than those for ring B. The aromatic C-H modes of ring A were calculated at 3086 and 3057–3079 cm^{-1} (exp. 3061 cm^{-1} and 2991–2946 cm^{-1}). The presence of the F-substituent increased the vibrational frequencies of the aromatic C-H modes.

The asymmetric C-H stretching modes of the N-CH3 groups were calculated at 3080 and 3029–2998 cm^{-1}, while, in the experimental spectrum, these stretching modes were observed at 3027, 2931, and 2920 cm^{-1}. The high-frequency C-H mode of the N-CH3 group appeared overlapped with the aromatic C-H modes. In contrast, the symmetric C-H modes of the N-CH3 groups were predicted at a lower frequency of 2966 cm^{-1} (exp. 2892 cm^{-1}) [45]. The asymmetric and symmetric C-H stretching vibrations of the methylene group were predicted

at 2998 and 2933 cm^{-1}, respectively. The $\nu_{(C10\text{-}H11)}$ and $\nu_{(C21\text{-}H22)}$ stretches were calculated at 2947 (exp. 2844 cm^{-1}) and 2983 cm^{-1}, respectively. The acidic C-H bond of the ring carbons appeared at very low wavenumbers in the IR spectra of the studied compounds. We found C-H stretching modes are pure and have a high TED%.

The umbrella vibrational modes are considered the most important bending vibrations of methyl groups. These modes usually detected in the range 1375 ± 10 cm^{-1}. The studied compound has two N-CH_3 groups with umbrella vibrations appeared at a higher frequency than expected, 1424 cm^{-1} (calc. 1423–1398 cm^{-1}). Moreover, the asymmetric C-H bending of the N-CH_3 group was calculated at 1465–1449 cm^{-1} (exp. 1440 cm^{-1}). The asymmetric bending vibrations of the N-CH_3 groups have higher wavenumbers than the symmetric modes. Other bending vibrations were found mixed with the C-C, C-N, and other bending vibrations (Table S4; Supplementary Data). The aromatic C-H in-plane bending modes were found in this overlapping region, while the out of plane C-H modes of the aromatic structure were predicted at lower frequencies of 976–696 cm^{-1} (exp. 969–705 cm^{-1})

2.12.2. Carbonyl vibrations

The carbonyl stretching vibration is considered one of the most intense bands in the IR spectra. The studied compound has four carbonyl groups, so four C=O stretching modes were predicted. The stretching vibrational wavenumbers of these carbonyl groups were calculated at 1743, 1692, 1685, and 1676 cm^{-1}. Experimentally, three ($\nu_{C=O}$) bands were detected at 1730, 1685, and 1674 cm^{-1}. The highest wavenumber band was predicted to have low vibrational intensity both experimentally and theoretically. This mode was predicted using the TED to arise from the symmetric C=O stretches of the three carbonyl groups. The remaining $\nu_{C=O}$ modes were strong and assigned to the asymmetric stretching vibrations.

2.12.3. C-C, C-N, and C-F vibrations

The aromatic stretching C-C modes ($\nu_{C\text{-}C}$) usually appears around 1600–1585 cm^{-1} and 1500–1400 cm^{-1}. The TED analyses of **3k** predicted the $\nu_{C\text{-}C}$ modes at 1589, 1572, 1570, and 1487 cm^{-1}. The breathing modes of rings A and B were calculated at 984 and 808 cm^{-1}, respectively, while the out of plane ring vibrations for rings A and B were calculated at 404 and 410 cm^{-1}, respectively. The C-N stretching modes of the pyrimidinetrione ring were

calculated using TED analysis at 1354, 1255, and 1229 cm^{-1}. The higher wavenumbers of these modes indicated the C-N bonds have some double bond characters due to the electron delocalization with the adjacent carbonyl groups. The aromatic ν_{C-F} stretching vibrations usually appeared in the region 1400–100 cm^{-1}. Experimentally this band was observed at 1216 cm^{-1}, while it was calculated at 1220 cm^{-1}. The CCF bending modes were calculated at 625, 425, and 387 cm^{-1} (exp. 619 and 439 cm^{-1}).

2.13. Biological activity

The synthesized monoalkylated barbiturate derivatives **3a–l** were screened *in vitro* for their antioxidant activity (DPPH radical scavenging ability) and *α*-glucosidase enzyme inhibition activity. The results of the bioassay studies are summarized in Table 7.

Table 7: Biological activity evaluation of compounds **3a-l**

#	**DPPH Radical Scavenging Assay IC_{50}±SEM[µM]**	**α-Glucosidase Inhibition Assay IC_{50}±SEM[µM]**
3a	314.127±2.4	NA
3b	91.223±0.75	133.1±3.2
3c	107.241±0.83	NA
3d	93.149±0.63	305±7.7
3e	112.084±0.55	184±2.3
3f	92.245±0.79	NA
3g	92.094±1.3	NA
3h	124.109±0.49	NA
3i	118.634±1.02	NA
3j	122.662±1.05	NA
3k	116.440±0.28	NA
3l	114.6±0.9	NA

ST D.	**Gallic acid** **23.436±0.43**	**Acarboses** **840±1.73**

2.13.1. Antioxidant activity (DPPH radical scavenging assay)

The synthesized monoalkylated barbiturate derivatives **3a–l** were evaluated for their antioxidant activity *in vitro* using the DPPH radical scavenging assay. These compounds were found to be weak scavengers of free DPPH radicals (IC_{50} = 91 ± 0.75 – 122 ± 1µM) compared to the standard, gallic acid (IC_{50} = 23 ± 0.43 µM). The 3-oxo-1,3-diphenylpropyl substituted pyrimidine adduct **3a** was found to be the least active member of the series (IC_{50} = 314 ± 2 µM). However a gradual increase in activity was observed for compounds **3h** (IC_{50} = 124 ± 0.49 µM), **3j** (IC_{50} = 122 ± 1µM), **3i** (IC_{50} = 118 ± 1µM), **3k** (IC_{50} = 116 ± 0.28µM), **3l** (IC_{50} = 114 ± 0.9 µM), **3e** (IC_{50} = 112 ± 0.55 µM), **3c** (IC_{50} = 107 ± 0.83 µM), **3b** (IC_{50} = 91 ± 0.75 µM), **3d** (IC_{50} = 93 ± 0.63 µM), **3f** (IC_{50} = 92 ± 0.79 µM), and **3g** (IC_{50} = 92 ± 1 µM), which contain fluoro, bromo, and chloro substituents on the phenyl rings of central 3-oxo-1,3-diphenylpropylpyrimidine backbone.

2.13.2. α-Glucosidase inhibition activity

The monoalkylated barbiturate derivatives **3a–l** were also evaluated for their *in vitro* α-glucosidase inhibiting activities compared to the standard drug acarbose (IC_{50} = 840 ± 1.73 µM). Compound **3a**, which contains a diphenyl substituted 3-oxo-propyl chain, was inactive against the enzyme. In contrast, high activities were observed for compounds **3b**, **3d**, and **3e**, which contain *para*-nitrophenyl (**3b**, IC_{50} = 133.1 ± 3.2 µM), *meta*-bromophenyl (**3d,** IC_{50} = 305 ± 7.7 µM), and thiophene rings (**3e**, IC_{50} = 184 ± 2.3 µM) attached to the central 3-oxo-1,3-dipropyl substituted pyrimidine skeleton. These compounds exhibited more activity than the tested standard acarbose (IC_{50} = 841 ± 1.73 µM). All other compounds were found to be inactive. The complete absence of activity may be due to the positional difference of substituents between different compounds, such as **3c**, which has an *ortho*-nitrophenyl ring instead of a *para*-nitrobenzene ring (**3b**). Interestingly all barbiturates with fluoro or chloro-substituted phenyl rings (**3f**–**3l)** were inactive in this assay.

2.14. Molecular docking

To predict the interaction of these newly synthesized compounds in the *α*-glucosidase binding pocket, we docked the most potent compound (**3b**) with this enzyme [18, 46]. From the docking simulation, we found that compound **3b** fitted well into the α-glucosidase binding cavity, forming interactions with the residues His 279 and Asn 241. His 279 forms an arene-cation interaction with the phenyl moiety of the compound, whereas Asn 241 forms a hydrogen bond with the carbonyl oxygen of pyrimidine moiety of the compound. Additionally, several hydrophobic interactions between the compound and active site residues (e.g., Phe 157, Ala 278, and Phe 311) were observed (Fig. 6).

In case of the second most active compound (compound **3e**) in the series the docking results showed that a hydrogen bond was established between the carbonyl oxygen atom of the compound and nitrogen atom of the active site residue Asp 349 whereas the phenyl ring of the compound formed an arene-cation interaction with active site residue Arg 312. A number of hydrophobic interactions were also observed between the compound **3e** and hydrophobic residues present in the active site (e.g., Phe157 and Phe Phe311) (Fig. 7).

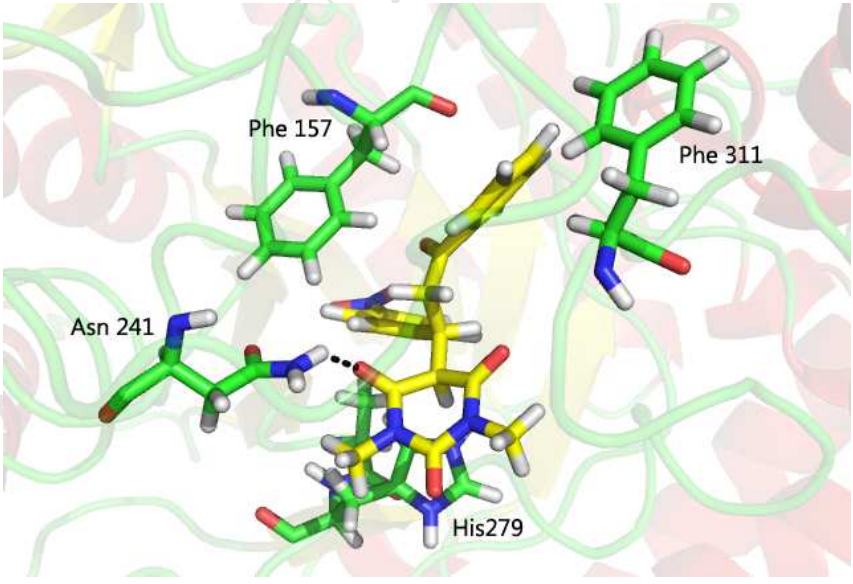

Fig. 6. Docking pose of the compound **3b** in the active site of α-glucosidase enzyme

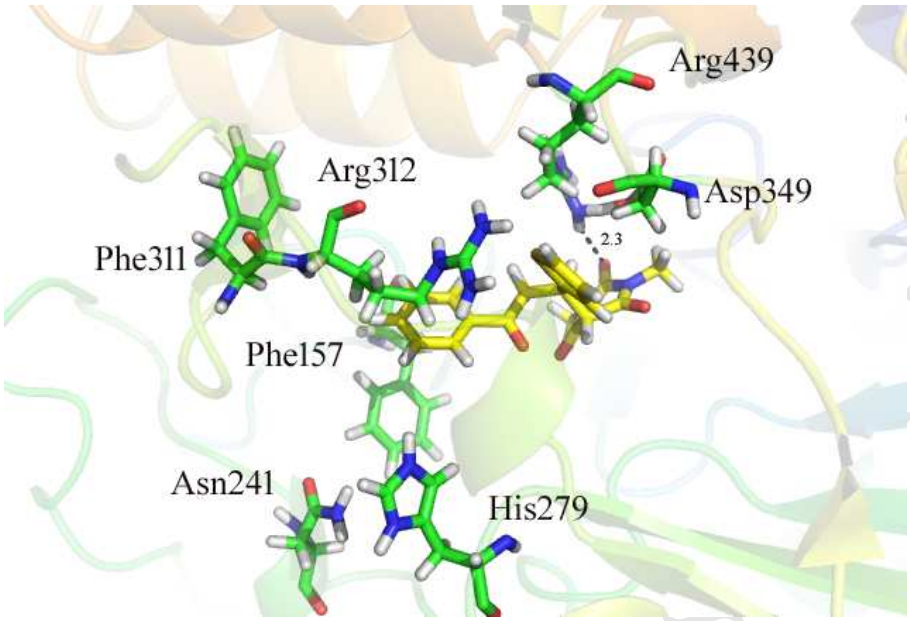

Fig. 7. Docking pose of the compound **3e** in the active site of α-glucosidase enzyme.

The docking result of the least active compound (compound **3d**) of the series showed only one interaction with the active site residues. This compound showed a hydrogen bond with the active site residue Asn 347 but no anre-arene or arene-cation interaction were observed (Fig. 8). This might be one of the reasons for this compound to show less activity as compare to compound **3b** and **3e**.

In case of inactive compounds (compound **3h**) no significant interaction with the active site residues of the enzyme was observed (Fig. 9).

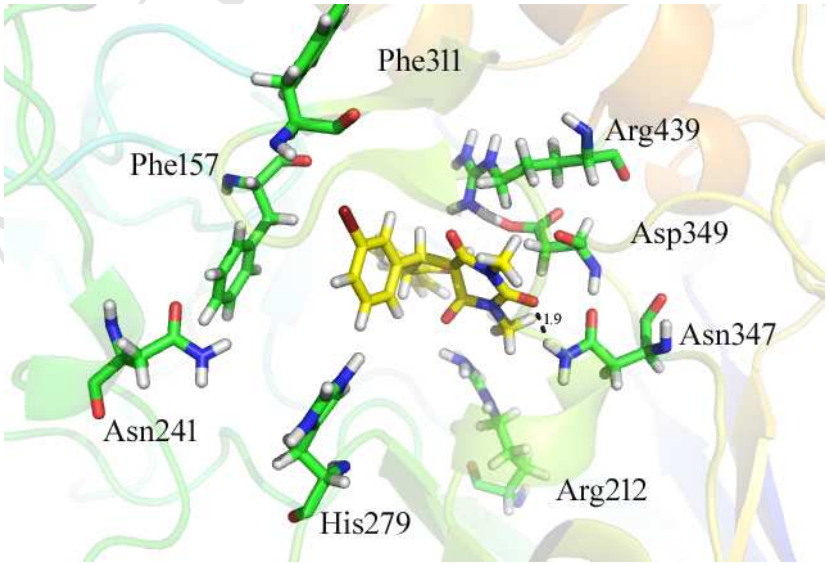

Fig. 8. Docking pose of the compound **3d** in the active site of α-glucosidase enzyme.

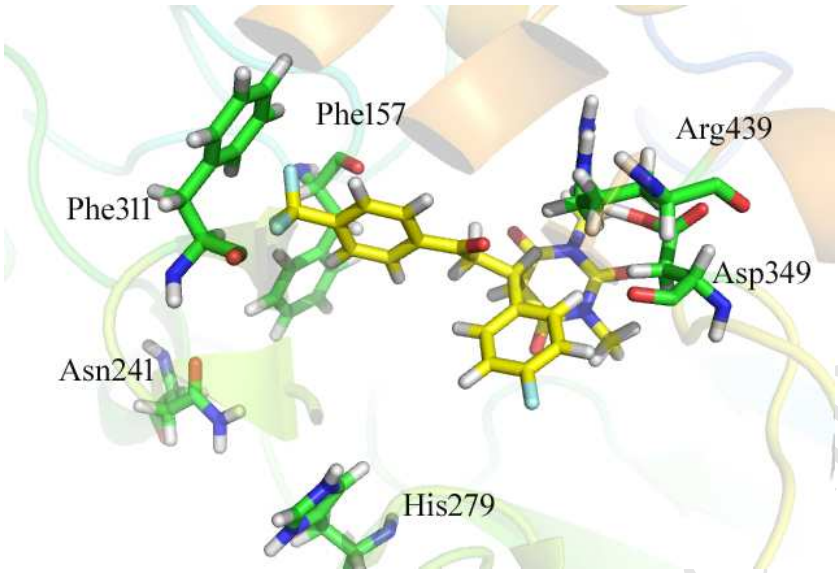

Fig. 9. Docking pose of the compound **3h** in the active site of α-glucosidase enzyme.

3. Materials and Methods

3.1. General remarks

"All the chemicals were purchased from Aldrich, Sigma-Aldrich, and Fluka and were used without further purification, unless otherwise stated. All melting points were measured on a Gallenkamp melting point apparatus in open glass capillaries and are uncorrected. IR spectra were measured on KBr pellets on a Nicolet 6700 FT-IR spectrophotometer. The NMR spectra were recorded on a Varian Mercury Jeol-400 NMR spectrometer. ^{1}H-NMR (400 MHz) and ^{13}C-NMR (100 MHz) were run in either deuterated dimethyl sulfoxide (DMSO-d_6) or deuterated chloroform ($CDCl_3$). Chemical shifts (δ) are in ppm, and *J*-coupling constants are given in Hz. Mass spectra were recorded on a Jeol JMS-600 H. Elemental analysis was carried out on Elmer 2400 Elemental Analyzer in CHN mode. For X-ray diffraction analysis, data were collected on a Bruker APEX-II D8 Venture diffractometer with an area detector. The electronic spectrum of **3k** was measured using a Perkin Elmer, Lambda 35, UV/Vis spectrophotometer".

3.2. General Michael addition reaction for the synthesis of pyrimidine derivatives 3a–l (GP1).

The compounds were prepared using our previously reported method [17].

3.3. X- ray crystallography

Crystals of compound **3k** were obtained by the slow diffusion of a diethyl ether solution of pure compound **3k** in dichloromethane at room temperature for 24 h. Data were collected on a Bruker APEX-II D8 Venture diffractometer equipped with a graphite monochromator and Cu Kα radiation at 293(2)K. Cell refinement and data reduction were carried out using Bruker SAINT. SHELXS-97 [22, 23] was used to solve the structure. The final refinement was carried out by full matrix least squares refinement. Non-hydrogen atoms were refined anisotropically. All the hydrogen atoms were placed in calculated positions.

3.4. Bioassays

3.4.1. DDPH radical scavenging assay:

A DPPH solution (95 µL, 300 µM) in ethanol was mixed with test solution (5 µl, 500 µM). The reaction was allowed to progress for 30 min at 37 °C, and the absorbance at 517 nm was monitored using a multiplate reader (SpectraMax340). Upon reduction, the color of the solution faded from violet to pale yellow. Percent radical scavenging activity (% RSA) was determined by comparison with a DMSO-containing control. The IC_{50} values of compounds were calculated using the EZ-Fit enzyme kinetics program (Perrella Scientific Inc., Amherst, MA, USA). *N*-Acetylcysteine, ascorbic acid, and BHA were used as reference compounds [47].

3.4.2. In vitro α-glucosidase inhibition assay.

First, 135 µL of a 50 mM phosphate saline buffer pH (6.8) was dispensed in a 96-well plate. Then, 20 µL of the test sample in 70% DMSO was dispensed into the wells. Subsequently, 20 µL of the enzyme was added to the wells, and the plate was incubated for 15 min. After incubation, the plate was pre-read using the spectrophotometer. After the pre-read, 25 µL of the substrate (ÞNPG) was added, and readings were taken again at 400 nm for 30 minutes. Finally, a normal read was taken, and the percent inhibition was calculated [48,49].

3.5. Molecular docking

Docking of the 5-monoalkylbarbiturate derivatives against α-glucosidase was carried out using the Molecular Operating Environment (MOE 2010.11). The same protocol was used for the protein, ligand preparation, and molecular docking, as described in our previous papers [18–46].

4. Conclusions

In summary, we have synthesized a series of 5-monoalkylbarbiturate derivatives *via* Michael addition reaction mediated by $NHEt_2$ in CH_2Cl_2. Using DFT calculations at the B3LYP/6-311G(d,p) level of theory, we have optimized the X-ray structure. The final optimized structure is in good agreement with the experimental structure. The structural deviations between the models can be attributed to the differences between calculation and experimental measurements, i.e., gas phase and solid state. The IR spectrum of the studied compound was calculated and assigned based on the total energy distribution. The calculated UV-Vis spectrum of **3k** was compared with the experimental spectrum. The most intense and longest wavelength band was assigned to the H-2→L (80%) transition. The molecular orbital contribution showed that the most intense bands belong to π→π* transitions. A molecular electrostatic potential map and global reactivity parameters were used to describe the chemical reactivity of the studied molecule. The desired compounds were investigated *in vitro* for antioxidant activity (DPPH), and α-glucosidase inhibition with promising results.

Supplementary Materials: General procedure of the Michael addition reaction for the synthesis of pyrimidine derivatives **3a–l** (GP1). **Fig. S1** Comparison between the calculated and experimental bond distances of **3k**. **Fig. S2** Comparison between the calculated and experimental bond angles of **3k**. **Fig. S3** MEP map of **3k**. **Fig. S4** The HOMO and LUMO energy levels of **3k** calculated at the B3LYP/6-311G(d,p) level of theory. **Fig. S5** Experimental (upper) and theoretical (lower) electronic spectra of **3k** calculated using the TD-DFT method. **Fig. S6** Correlation graph between the experimental and calculated ^{1}H chemical shifts of **3k**. **Fig. S7** Correlation graph between the experimental and calculated ^{13}C chemical shifts of **3k**. **Fig. S8** The calculated scaled [45] IR vibrational spectra of **3k** at the B3LYP/6-311G(d,p) level of theory. **Fig. S9** The FTIR spectra of **3k**.

Acknowledgments: The authors would like to extend their sincere appreciation to the Deanship of Scientific Research at King Saud University for providing funding to this Research group NO (RGP -257).

Conflicts of Interest: "The authors declare no conflict of interest."

References

[1] E. Maquoi, N. E. Sounni, L. Devy, F. Olivier, F. Frankenne, H.-W. Krell, F. Grams, J.-M. Foidart and A. N¨oel, Clin. Cancer Res., 10(2004)4038–4047.

[2] A. S. Rao, and R. B. Mitra. Indian Journal of Chemistry 12(1974) 1028-1030.

[3] P. R. Andrews, L. C. Mark, D. A. Winkler and G. P. Jones, J. Med. Chem., 26(1983)1223–1229.

[4] N. D. McClenaghan, C. Absalon and D. M. Bassani, J. Am. Chem. Soc., 125(2003) 13004–13005.

[5] R. Andreu, J. Gar´ın, J. Orduna, R. Alcal´a and B. Villacampa, Org. Lett., 5(2003)3143–3146.

[6] H. Lee, M. Y. Berezin, K. Gou, J. Kao and S. Achilefu, Org. Lett., 11(2009)29–32.

[7] J. Wang, S. O'Sullivan, S. Harmon, R. Keaveny, M. W. Radomski, C. Medina and J. F. Gilmer, J. Med.Chem., 55(2012) 2154–2162

[8] J. C. Ruble, A. R. Hurd, T. A. Johnson, D. A. Sherry, M. R. Barbachyn, P. L. Toogood, G. L. Bundy, D. R. Graber and G. M. Kamilar, J. Am. Chem. Soc., 131(2009) 3991–3997.

[9] G. Xia, R. Benmohamed, J. Kim, A. C. Arvanites, R. I. Morimoto, R. J. Ferrante, D. R. Kirsch and R. B. Silverman, J. Med. Chem., 54(2011)2409–2421.

[10] I. Devi and P. J. Bhuyan, Tetrahedron Lett., 46(2005) 5727–5729.

[11] B. M. Trost and G. M. Schroeder, J. Org.Chem., 65(2000) 1569–1573

[12] B. S. Jursic and E. D. Stevens, Tetrahedron Lett.,44(2003)2203–2210

[13] C. Löfberg, R. Grigg, A. Keep, A. Derrick, V. Sridharan and C. Kilner, Chem. Commun., (2006) 5000–5002

[14] A. Volonterio and M. Zanda, J. Org. Chem., 73(2008)7486–7497.

[15] L. P. Zalukaev and V. L. Trostyanetskaya, Khim. Geterotsikl. Soedin., 6(1971)836–837.

[16] A. N. Osman, A. A. El-Gendy, M. M. Kandeel, E. M. Ahmed and M. M. M. Hussein, Bull. Fac. Pharm.,41(2003)59–68.

[17] A. Barakat, M.S. Islam, A.M. Al-Majid, S. M. Soliman, Y. N. Mabkhot, Z. A. Al-Othman, H. A. Ghabbour, and H-K. Fun. Tetrahedron Letters 56(2015) 6984-6987.

[18] A. Barakat, M.S. Islam, A.M. Al-Majid, H. A. Ghabbour, H-K. Fun, K. Javed, R. Imad, S. Yousuf, M.I. Choudhary, A. Wadood. Bioorganic & Medicinal Chemistry 23(2015)6740-6748

[19] A. Barakat, S. M. Soliman, A. M. Al-Majid, G. lofty, H. A. Ghabbour, H-K. Fun, S.Yousuf, M. I. Choudhary, Abdul Wadood. Journal of Molecular structure 1098(2015) 365-376.

[20] A.Barakat, S.M. Soliman, Y.A. Elshaier, M. Ali, A.M.Al-Majid, H.A. Ghabbour, Journal of Molecular Structure, 1134(2017)99–111.

[21] A.Barakat, M.S. Islam, A.M.Al-Majid, H.A. Ghabbour, S. Yousuf, M. Ashraf, N.N.Shaikh, M.I.Choudhary, R. Khalil, Z. Ul-Haq. Bioorganic Chemistry. 68(2016) 72-9.

[22] G.M. Sheldrick, ActaCrystallogr. A 64 (2008) 112–122.

[23] G.M. Sheldrick, SHELXTL-PC (Version 5.1), Siemens Analytical Instruments,Inc., Madison, WI, 1997.

[24] The structure of **3k**was determined by X-ray crystal structure analysis (Bruker AXS GmbH). CCDC- 1024287; contains the supplementary crystallographic data for this compound. These data can be obtained free of charge from the Cambridge Crystallographic Data Centre viawww.ccdc.cam.ac.uk/data_request/cif.

[25] M. J. Frisch, et al., Gaussian-03, Revision C.01, Gaussian, Inc., Wallingford, CT, (2004).

[26] G.A. Zhurko, D.A. Zhurko, Chemcraft Program Academic version 1.6, 2009.

[27] GaussView, Version 4.1, R. Dennington II, T. Keith, J. Millam, Semichem Inc., Shawnee Mission, KS, (2007).

[28] N.M.O. Boyle, A.L. Tenderholt, K.M. Langer, J. Comput. Chem. 29 (2008) 839–845.

[29] E.D. Glendening, A.E. Reed, J.E. Carpenter, F. Weinhold, NBO Version 3.1, CI,University of Wisconsin, Madison, (1998).

[30] R.G. Parr, L. Szentpaly, S. Liu, J. Am. Chem. Soc. 121 (1999) 1922–1924.

[31] P.K. Chattaraj, B. Maiti, U. Sarkar, J. Phys. Chem. A107 (2003) 4973–4975.

[32] R.G. Parr, R.A. Donnelly, M. Levy, W.E. Palke, J. Chem. Phys. 68 (1978) 3801–3807.

[33] R.G. Parr, R.G. Pearson, J. Am. Chem. Soc. 105 (1983) 7512–7516.

[34] R.G. Parr, P.K. Chattraj, J. Am. Chem. Soc. 113 (1991) 1854–1855.

[35] M. Nendel, K.N. Houk, L.M. Tolbert, E. Vogel, H. Jiao, P.V.R. Schleyer, J. Phys. Chem. A 102 (1998) 7191.

[36] C.H. Choi, M. Kertesz, J. Chem. Phys. 108 (1998) 6681.

[37] AusraVektatiene, J. Org. Chem. (2009) 321–322.

[38] I. Fleming, Frontier Orbitals and Organic Chemical Reactions, Wiley, London,1976.

[39] G. Frenking, A. Krapp, J. Comput. Chem. 28 (2007) 15–24.

[40] R.G. Parr, R.G. Pearson, J. Am. Chem. Soc. 105 (1983) 7512–7516.

[41] R.G. Parr, L. Szentpaly, S. Liu, J. Am. Chem. Soc. 121 (9) (1999) 1922–1924.

[42] K. Pihlaja, E. Koleinpeter (Eds.), Carbon-13 Chemical Shifts in Structural and Stereochemical Analysis, VCH Publishers, Deerfield Beach, 1994.

[43] M.H. Jamròz, Vibrational Energy Distribution Analysis VEDA 4, Warsaw, 2004.

[44] S. P. V. Chamundeeswari, E. R. J. J. Samuel, N. Sundaraganesan Europ. J. Chem. 2 (2) (2011) 136-145.

[45] Brian C. Smith, Infrared Spectral Interpretation: A Systematic Approach, *CRC Press Boca Raton London* New York Washington, 2000.

[46] V.M.Thadhani, M.I.Choudhary, S.Ali, I.Omar, H.Siddique, V.Karunaratne, Nat. Prod. Res., 25(19) (2011) 1827-1837.

[47] K.Yamamoto, H.Miyake, M.Kusunoki, Osaki S., FEBS J. 277 (2010) 4205.

[48] E. Baydoun, M. Karam, Atia-tul-Wahab, M.S. Khan , M.S. Ahmad, Samreen, C. Smith , R. Abdel-Massih, M.I. Choudhary,Steroids. 88 (2014) 95-100.

[49] C.Lee, M. B.Yim, P. B. Chock, H. S.Yim, S. O. Kang, Journal of Biological Chemistry, 273 (39)(1998)25272-25278.

Highlights

- A series of 5-monoalkylated barbiturate derivatives **3a-l** were prepared.
- *In vitro* biological evaluation of **3a-l** was described.
- Molecular docking was also investigated for the compound **3b**.
- X-Ray crystal structure of **3k** was reported.
- The electronic and spectroscopic properties of **3k** were predicted using DFT method.